Materials Futures

PAPER • OPEN ACCESS

Electrochemically stable and ultrathin polymer-based solid electrolytes for dendrite-free all-solid-state lithium-metal batteries

To cite this article: Fenghua Yu *et al* 2025 *Mater. Futures* **4** 015101

View the article online for updates and enhancements.

You may also like

- Transition from Vogel-Fulcher-Tammann to Arrhenius Ion-Conducting Behavior in Poly(Ethyl Acrylate)-Based Solid Polymer Electrolytes via Succinonitrile Plasticizer Addition
Lei Wang, Yubin He and Huolin L. Xin

- High-power, stable single-mode CW operation of 1550 nm wavelength InP-based photonic-crystal surface-emitting lasers
Takeshi Aoki, Yuhki Itoh, Kosuke Fujii et al.

- Para-Cresyl Sulfate and BSA Conjugation for Developing Aptasensor: Spectroscopic Methods and Molecular Simulation
Payal Gulati, Awadhesh kumar Verma, Anil Kumar et al.

This content was downloaded from IP address 112.232.226.26 on 17/01/2025 at 02:01

OPEN ACCESS
IOP Publishing | Songshan Lake Materials Laboratory

MATERIALS FUTURES

Mater. Futures 4 (2025) 015101 (11pp)

https://doi.org/10.1088/2752-5724/ada0cc

Electrochemically stable and ultrathin polymer-based solid electrolytes for dendrite-free all-solid-state lithium-metal batteries

Fenghua Yu[1,2], Yongbiao Mu[1,2], Meisheng Han[1,2,*], Jie Liu[1,2], Kunxiong Zheng[1,2], Zhiyu Zou[1,2], Hengyuan Hu[1,2], Quanyan Man[1,2], Wenjia Li[1,2], Lei Wei[1,2], Lin Zeng[1,2,*] and Tianshou Zhao[1,2,*]

[1] Shenzhen Key Laboratory of Advanced Energy Storage, Department of Mechanical and Energy Engineering, Southern University of Science and Technology, Shenzhen 518055, People's Republic of China
[2] SUSTech Energy Institute for Carbon Neutrality, Southern University of Science and Technology, Shenzhen 518055, People's Republic of China

E-mail: hanms@sustech.edu.cn, zengl3@sustech.edu.cn and zhaots@sustech.edu.cn

Received 31 October 2024, revised 9 December 2024
Accepted for publication 17 December 2024
Published 16 January 2025

Abstract

Polymer-based composite solid electrolytes (PCSEs) are increasingly studied in all-solid-state lithium-metal batteries (ASSLMBs) due to the combined advantages of better flexibility of polymer and higher ion conductivity of ceramic electrolytes. However, most reported PCSEs are overly thick, increasing internal resistances. Besides, the poor stability at the Li metal–electrolyte interfaces often leads to severe lithium dendrite formation and reduced cycling stability. Here, we fabricate an ultrathin PCSE with a thickness of 12.4 μm, incorporating polyacrylonitrile (PAN) nanofibers as the structural matrix, and a filler with polyethylene oxide and $Li_{6.5}La_3Zr_{1.5}Ta_{0.5}O_{12}$ (LLZTO). Due to the formation of the LiCN layer on the surface of the lithium metal and the Li-ion transport pathways induced by the dehydrocyanation reaction at the LLZTO/PAN interfaces, the PCSE exhibits a high critical current density of 1.8 mA cm^{-2} and a low energy barrier of 0.278 eV for Li-ion transfer, accommodating the fast Li-ion migration to avoid Li-dendrite growth. In addition, the stable nitrile groups and the dehydrocyanation reaction ensure the electrochemical stability of the PCSE with a high oxidation voltage of 5.5 V and an exceptional cycling stability (2100 h) in Li||PCSE||Li symmetric cells. Additionally, the Li||PCSE||$LiFePO_4$ full cells demonstrate a high volumetric energy density of 338.3 Wh L^{-1} at 0.1 C and a robust stability over 100 cycles at 0.5 C. The study offers a new approach for fabricating ultrathin PCSEs and provides insights into the mechanisms of dendrite-free formation, guiding the development of high-performance PCSEs for ASSLMBs.

* Authors to whom any correspondence should be addressed.

Original content from this work may be used under the terms of the Creative Commons Attribution 4.0 licence. Any further distribution of this work must maintain attribution to the author(s) and the title of the work, journal citation and DOI.

© 2025 The Author(s). Published by IOP Publishing Ltd on behalf of the Songshan Lake Materials Laboratory

Supplementary material for this article is available online

Keywords: polymer-based composite solid electrolytes, all-solid-state lithium-metal batteries, interfacial stability, ultrathin thickness, dendrite-free growth

1. Introduction

Lithium-ion batteries (LIBs) are facing safety issues due to explosion risks associated with organic liquid electrolytes [1]. Besides, the LIBs, with limited energy density, are restricted in the duration of electrical applications. To tackle these challenges, one efficient approach is to substitute organic liquid electrolytes with nonflammable and highly safe solid-state electrolytes (SSEs) [2, 3]. The SSEs can mitigate the growth of lithium dendrites to make it practical to apply for all-solid-state lithium-metal batteries. The configuration significantly increases energy density due to a higher capacity of 3860 mAh g^{-1} for lithium-metal anodes [4, 5] than 372 mAh g^{-1} of graphite anodes.

SSEs are generally classified into ceramic electrolytes (CEs), polymer electrolytes (PEs), and polymer-based composite solid electrolytes (PCSEs) [6]. CEs, including $Li_7La_3Zr_2O_{12}$ (LLZO) [7], $Li_{6.5}La_3Zr_{1.5}Ta_{0.5}O_{12}$ (LLZTO) [8], $Li_{10}GeP_2S_{12}$ (LGPS) [9, 10], and $Li_{1.3}Al_{0.3}Ti_{1.7}(PO_4)_3$ (LATP) [11, 12], are noted for high tensile modulus, which helps suppress lithium dendrite formation. They also offer excellent ionic conductivity, thereby minimizing ohmic losses. However, the inherent rigidity of CEs limits their application in wearable devices. Furthermore, their thickness is challenging to be reduced below 20 μm with the conventional tableting method, which often results in a thickness exceeding 100 μm. The thickness of SSEs increases, accompanied by ionic conductivity decreasing and energy density diminishing because of the additive extra materials. Moreover, it is also challenging to tackle the severe problems in solid–solid interfacial contact [13–15]. The wettability between CEs and Li metal is proposed as the crucial feature in ASSBs [16]. The ion conduction process also causes a lattice disorder, which induces micro-cracks, allowing dendrite growth. By contrast, the lithium salt and the chemical properties of polymer limit the ionic conductivity. Although PEs offer desirable properties such as flexibility and the available thin film casting method, the lower mechanical strength, with a tensile modulus around 1 MPa, limits their suppression of lithium dendrites. The PCSEs aim to merge the benefits of both CEs and PEs, which results in an acceptable ionic conductivity, flexibility, and a suitable tensile modulus (10–60 MPa).

Among CEs, the LLZTO with exceptional lithium-ion (Li^+) conductivity is commonly used in PCSEs. Polyethylene oxide (PEO)-based PCSEs benefit from self-healing properties, helping address cracks and extending the lifespan of the SSEs. The addition of lithium salts to PEO reduces its crystallinity, thereby enhancing ionic conductivity by decreasing the mobility of EO segments [17]. Furthermore, metal oxide fillers like LLZTO slightly increase the modulus of PEO-based SSEs through hydrogen bonding with the PEO matrix [18]. In addition, it is also essential to provide a strong frame to enhance the tensile modulus. Among various polymers, polyacrylonitrile (PAN) stands out due to its high tensile modulus, which enhances the mechanical performance of PCSEs. The interaction between PAN and LLZTO further optimizes the Li^+ conducting mechanism, providing additional benefits to the performance of these electrolytes [19–21].

Recent studies explored PEO/LLZTO-based PCSEs to improve interfacial stability on the anode side and ionic conductivity by creating Li^+ transport pathways and chemical reactions to stabilize the interfaces [22]. Stable interfaces with the formation of LiCN at Li-metal side are widely developed [23, 24]. For instance, Zhang *et al* found that the chemical interaction between PAN and LLZTO induces dehydrocyanation, creating local Li^+ conductive conjugates and achieving an activation energy (E_a) of 0.36 eV [18]. Yan *et al* reported that additives (bismuth (III) triflate) weaken Li-EO coordination, enhancing stability and ionic conductivity. Additionally, high-voltage cathodes with modified PEO-based electrolytes enable symmetric cells to reach a critical current density (CCD) of 1.2 mA cm^{-2} [25]. Yin *et al* demonstrated that embedding PEO-based electrolytes in a 3D aramid nanofiber framework provides both high ionic conductivity and chemical stability, achieving an oxidation voltage of 5.25 V [26]. Gao *et al* showed that incorporating a high content of LLZTO in PCSEs reduces the crystallinity of lithium bis(trifluoromethanesulfonyl)imide (LiTFSI), which, along with plasticizer succinonitrile (SN) and liquid electrolyte wetting, results in an E_a of 0.39 eV [27]. PCSEs often exhibit ionic conductivities in the range of 10^{-4}–10^{-6} S cm^{-1} when using oxide ceramic materials [28]. Research reported that SSE with a thickness of around 15 μm through tape-casting methods can greatly reduce internal impedance [29, 30]. Nevertheless, issues such as uneven component distribution [31] and rough surfaces caused by the coffee-ring effect [32] are common challenges in this process. The short cycling life is often caused by lithium dendrite growth and rough surface on the micro-scale. To address these problems, techniques like side-by-side solvent evaporation can be employed to ensure a smoother surface on the substrate side,

while suction filters can aid in achieving a more uniform composition of the slurry and frame. Despite these challenges, unnecessary additives are often added to the PCSEs, accompanied by extra costs.

Here, we develop an ultrathin PCSE using PAN fibers as the structural matrix and a filler combination of PEO, LLZTO, and LiTFSI, which is labeled as POLL. To compare, we also prepared two other types of PCSEs: OLL, which lacks PAN, and PLL, which omits LLZTO. POLL performs apparently well in improving the interfacial stability and Li-dendrite suppression due to its high tensile modulus of 20.6 MPa and smooth uniform surface. The impressive thickness of 12.4 μm also decreases internal resistances. In addition, the POLL possesses a stable Li^+ conduction pathway, a low energy barrier for Li^+ transfer, and a high oxidation voltage of 5.5 V due to the vital dehydrocyanation reaction with nitrile groups in the PAN. The uniformity of each component in the PCSE induces an even charge distribution at the lithium metal–electrolyte interfaces, and the ultrathin thickness contributes to a low overall resistance. Moreover, the low activation energy, which determines the activation polarization, also requires a low applied voltage to conduct Li^+. With a uniform and low overpotential distribution at the interfaces of lithium metal–electrolyte, the POLL suppresses the occurrence of side reactions and the growth of lithium-dendrite. The high oxidation voltage implies an electrochemically stable interaction in the POLL, further restricting unfavorable decomposition reactions on the POLL. The suppression of lithium dendrite growth is attributed to the formation of a stable LiCN phase at the lithium metal–electrolyte interfaces. The Li^+ pathway promoted by the polar nitrile group and dehydrocyanation reaction significantly enables Li symmetric batteries with POLL to achieve a high CCD of 1.8 mA cm^{-2} at 60 °C and operate stably over 2100 h at 0.1 mA cm^{-2} and 0.1 mAh cm^{-2} at 60 °C. Besides, the Li||PCSE||$LiFePO_4$ batteries show a high volumetric energy density of 338.3 Wh L^{-1} at 0.1 C and maintain a stable performance over 100 cycles at 0.5 C at 60 °C.

2. Experimental section

2.1. Preparation of PAN nanofiber frame

The electrospinning technique is applied to fabricate the PAN nanofiber frame. 10 wt% PAN powder (Aladdin, M_w = 150 000) was dissolved in N, N-dimethylformamide (Macklin, 99.9%) solution uniformly. The electrospinning voltage was set at +16 kV and −2 kV with a spinning distance of 100 mm. The solution injection rate was 0.8 ml h^{-1}. The PAN thickness can be controlled by varying the electrospinning time. The obtained PAN frame was dried in the oven at 60 °C for 12 h.

2.2. Preparation of POLL

The slurry was mixed from PEO (Aladdin, M_w = 600 000), LLZTO, and LiTFSI (DodoChem) in acetonitrile (ACN, Macklin, 99.5%). The stirring step was under 60 °C for 12 h, in which the mass ratio was fixed at 1:1:1, and the mass of ACN was 10 times that of PEO. Covered on the surface of the suction filter, the PAN frame was poured on 3 ml slurry on each side with the negative pressure fixed at 0.5 bar for 30 s. The wet PCSE was transferred onto a Teflon substrate on a heating plate and placed in the glove box, which was dried at 60 °C for 48 h. Finally, the obtained PCSE was cut into φ16 mm disks and stored in an Ar-protected glovebox.

More experimental details can be referred to in the supporting information.

2.3. Calculation of volumetric energy density

The active LFP, active Li-metal, and PCSE thickness are taken into consideration. The mass loading is set as 1.5 mg cm^{-2}. The following formula is used for volumetric energy density calculation:

$$\text{volumetric energy density} = \frac{c \times m \times U}{S \times h}$$

where c is the specific capacity in the experiment, m is the mass loading, and U is the voltage at the medium capacity. S represents the active area of the electrodes, which can be calculated based on the diameter of circle slice (12 mm), and h is the total thickness of active materials.

3. Result and discussion

The POLL was fabricated as described in figure 1(a). Initially, a PEO/LLZTO/LiTFSI slurry was prepared and combined with an electrospun PAN fiber frame using suction filtration. Then, it was dried at 60 °C under a vacuum. Scanning electron microscope (SEM) images are used to assess the smoothness and thickness of the SSEs. Before slurry compositing, the PAN frame shows a uniform fiber distribution (figure 1(b)), which supports close chemical interactions with PEO/LLZTO/LiTFSI in the following steps. Post-compositing, the POLL displays a flat and smooth surface (figure 1(c)), which enhances the interfacial contact with electrodes by minimizing point-to-point contact. In contrast, the OLL and PLL show less satisfying surfaces. OLL shows solvent bubbles within the electrolyte (figure 1(d)), which can facilitate Li-dendrite growth and cause micro short-circuits [33]. The solvent bubbles are effectively managed in POLL due to PAN's infiltration and evaporation, preventing porous structures and ensuring a dense, mechanically, and electrochemically stable SSE. PLL, lacking LLZTO support, experiences shrinkage along fibers (figure S1(a)), leading to poor electrode contact and random interspaces.

Despite its smooth surface, the thickness of the SSEs is crucial for reducing overall impedance. Cross-sectional SEM images reveal that while the thickness of the PAN frame is about 410 μm (figure 1(e)), the resultant SSEs, including POLL and PLL, achieve thicknesses of less than 25 μm due

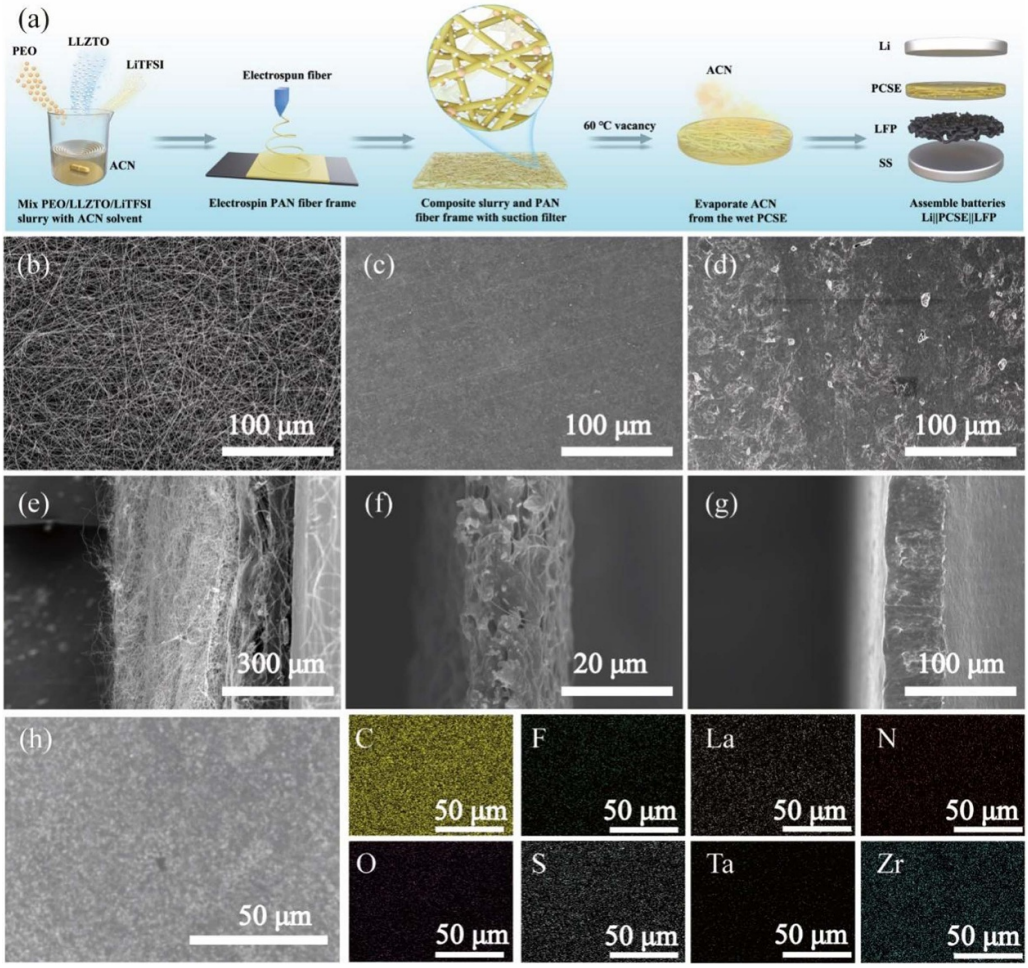

Figure 1. (a) Scheme of the fabrication process of POLL. (b)–(d) SEM images of PAN (b), POLL (c), OLL surfaces (d), (e)–(g) SEM images of the cross-section of PAN (e), POLL (f), OLL (g). (h) EDS image and its corresponding elemental distribution within a POLL surface SEM image region.

to slurry surface tension. In practice, POLL is around 12.4 μm thick (figure 1(f)), and PLL is about 24.9 μm (figure S1(b)). Thickness also impacts flexibility; for instance, POLL can be folded without cracking (figure S2), whereas OLL, being more brittle, has a practical thickness of around 54.2 μm (figure 1(g)) if transferred from its substrate. The EDS images also illustrate the uniform distribution of each component element of POLL (figure 1(h)), further indicating that PEO, LLZTO, and LiTFSI are located uniformly into the PAN frame. The uniformity, coupled with SEM observations, suggests few morphological defects, reducing the risk of lithium dendrite growth and promoting effective chemical interactions and stable Li^+ transport pathways.

Figure 2(a) presents the thermogravimetric analysis (TGA) curves of various SSEs. POLL, which contains moisture-sensitive LiTFSI, shows mass loss due to water evaporation up to 107 °C and remains stable until the beginning of decomposition at 317 °C. The high decomposition temperature indicates that the POLL is significantly more stable than the pure PAN frame, which reacts with air starting at 212 °C, providing a safer margin of 105 °C and making POLL particularly suitable for ASSBs, especially in extreme conditions. The ceramic LLZTO exhibits mass loss primarily from water evaporation at temperatures below 100 °C, suggesting that LLZTO should be stored under dry conditions, followed by carbonate decomposition and lithium evaporation at higher temperatures. Now that the lithium dendrite proliferation often accompanies the dislocation of materials [34], POLL demonstrates a tensile modulus of 20.6 MPa, reflecting its ability to suppress lithium dendrite growth. In contrast, OLL and PLL have a lower tensile modulus of 3.3 and 3.1 MPa, respectively (figure 2(b)). The high tensile modulus of POLL enhances its mechanical strength and pressure capability, favoring dendrite suppression even at an ultrathin thickness (12.4 μm).

The linear sweep voltammetry (LSV) test (figure 2(c)) demonstrates that POLL offers superior electrochemical stability, with a potential window extending from 2 to 7 V. POLL has a higher electrochemical window (5.5 V) than 4.0 V of OLL and 5.1 V of PLL. The broader window means that POLL is less prone to decompose in high-voltage battery systems and can better handle voltage fluctuations during overcharging. The enhanced stability is largely due to the stronger chemical interactions induced by the dehydrocyanation reaction between LLZTO and PAN, whereas SSEs

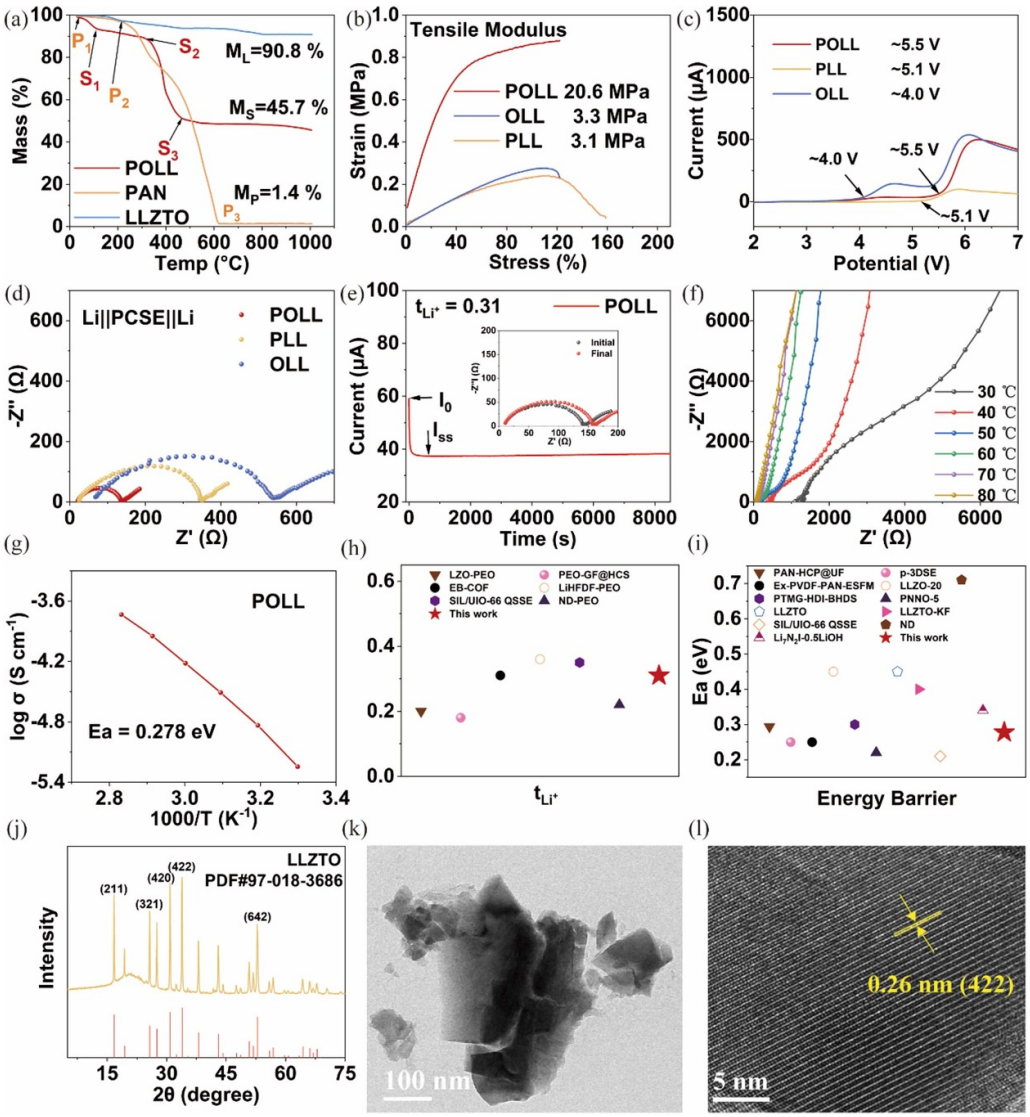

Figure 2. Intrinsic electrochemical properties of SSEs. (a) TGA curves of POLL and each necessary component. (b) The strain–stress curves of POLL, OLL, and PLL. (c) LSV plots of decomposition voltage. (d) Impedance of Li-symmetric cells with different SSEs. (e) *i–t* curve with 10 mV applied bias and impedance of initial and final state. (f) Nyquist plots of POLL assembled in stainless steel-symmetric cell at temperatures from 30 °C to 80 °C and (g) the corresponding Arrhenius plot of POLL. (h) t_{Li^+} comparison of SSEs. (i) Activation energy comparison of SSEs. (j) XRD pattern of LLZTO. (k), (l) TEM images of LLZTO.

without PAN or LLZTO oxidize at lower voltages. Benefiting from the ultrathin thickness, the POLL performs 140 Ω in the Li symmetric batteries (figure 2(d)), inheriting the outstanding ionic conductivity of LLZTO cooperating with the polar Li^+ transport pathway provided by the nitrile group [35]. In contrast, the PLL and OLL exhibit higher impedances of 348 and 539 Ω, respectively, potentially leading to increased overpotential and reduced energy efficiency. The control samples without LiTFSI or PEO may not perform well at 60 °C (figure S3). The SSEs without LiTFSI provide an ultrahigh impedance value of ∼50 000 Ω (figure S3(a)) and can only provide acceptable impedance values of ∼1783, ∼1287, and ∼785 Ω at 80 °C, 90 °C, and 100 °C, respectively (figure S3(b)). This is because the shortage of lithium ions increases the impedance of the electrolyte. Additionally, the slurry without PEO is not stably uniform (figure S3(c)), which easily leads to manufacturing failure. SSEs without PEO cannot be tested for impedance (figure S3(d)), on the grounds of lacking necessary close electrochemical contact brought by PEO. POLL also has a high lithium transference number (t_{Li^+}) of 0.31 (figure 2(e)), surpassing 0.03 of OLL (figure S4(a)) and 0.21 of PLL (figure S4(b)), and achieves steady-state conditions most rapidly under a 10 mV applied bias. With a practical t_{Li^+}, POLL is proven to have an effective and fast Li^+ transport pathway [36]. The activation energy (E_a), calculated from Nyquist (figures 2(f), S5(a) and (b)) and Arrhenius plots (figures 2(g), S5(c) and (d)), is 0.278 eV for POLL, lower than the 0.384 and 0.406 eV for OLL and PLL, respectively. A higher t_{Li^+} and a lower E_a benefit for a faster lithium-ion transport. The transference number is comparable among the recently reported PCSEs (figure 2(h), table S1). The activation energy of POLL is also comparable to

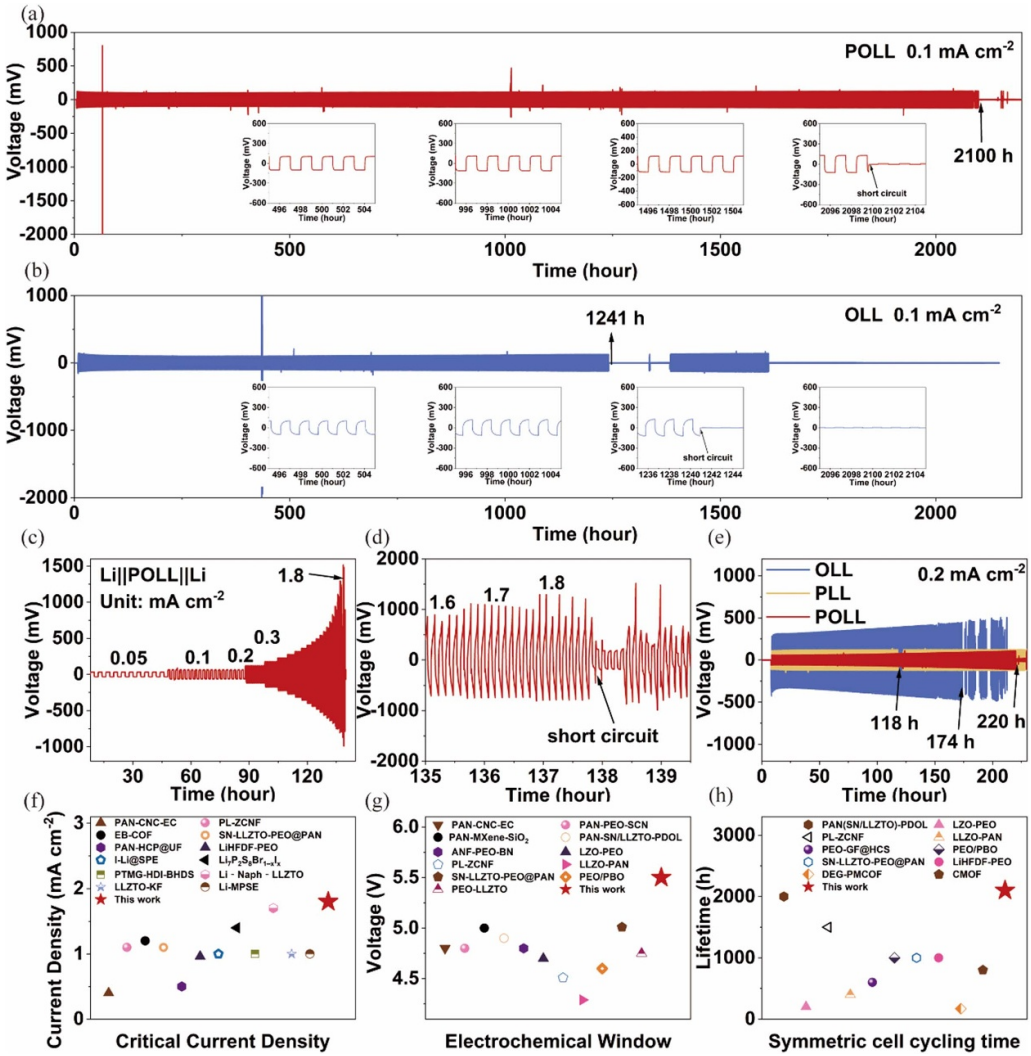

Figure 3. (a), (b) Li-symmetric cells cycling of POLL and OLL under 0.1 mA cm^{-2} with details at the selected time; (c), (d) CCD test of POLL and detailed plot near the critical point. (e) Li-symmetric cells cycling of POLL, OLL, and PLL under 0.2 mA cm^{-2} with various lifetime. (f)–(h) Comparison of CCD (f), electrochemical window (g), and cycling time (h) with recently reported articles.

those of recent researches, which means that the overpotential caused by activation polarization can be restricted (figure 2(i), table S2). Both XRD and TEM analysis confirms LLZTO's crystal structure (PDF#97-018-3686) with interplanar spacings of 0.53, 0.35, 0.29, 0.26, and 0.17 nm, corresponding to lattice indices (211), (321), (420), (422), and (642), respectively (figures 2(j)–(l)).

The cycling of Li–Li symmetric cells using POLL, PLL, and OLL were tested to evaluate the interfacial stability. Notably, all cells were tested without adding any liquid electrolyte. As illustrated in figure 3(a), the POLL has an ultralong cycle lifetime of 2100 h, during which the overpotential is stable around 0.1 V under a current density of 0.1 mA cm^{-2}. However, that of OLL is 1241 h (figure 3(b)), around half of POLL. The noticeable fluctuations in figures 3(a) and (b) are caused by the power supply failure of the lab and may not be considered in the analysis of the result. The PLL only experiences 418 h before the short circuit (figure S6). It is also apparent that the response time to reach the voltage steady state under a specific current density differs. The POLL attains the steady state more rapidly than OLL and PLL, which means that the Li^+ transfers more stably with less resistance, favoring a higher CCD and better rate performance in Li-symmetric cells and Li-LFP full cells. The impedance and the transference number also explain the response time and difficulty in Li^+ transfer, as shown in previous figures in figures 2(d) and (e). Apart from the cycling life, the CCD is also vital for evaluating ion transportation ability. The symmetric cells were tested from 0.05 to 2.0 mA cm^{-2} and 10 cycles per current density (20 cycles for 0.1 mA cm^{-2}) (figure 3(c)). From the figure 3(d), the CCD of POLL is 1.8 mA cm^{-2}. The CCD of PLL and OLL approach only 1.0 and 1.5 mA cm^{-2}, respectively. The high CCD of POLL enables a high Li^+ flux to pass it, potentially favoring for higher rate performance in Li-LFP full cells. The symmetric cells under 0.2 mA cm^{-2} also exhibit 220 hour life with POLL, while the OLL and PLL hold about 174 and 118 h, respectively (figure 3(e)). The previously reported PCSEs were fabricated with oxide ceramics like doped

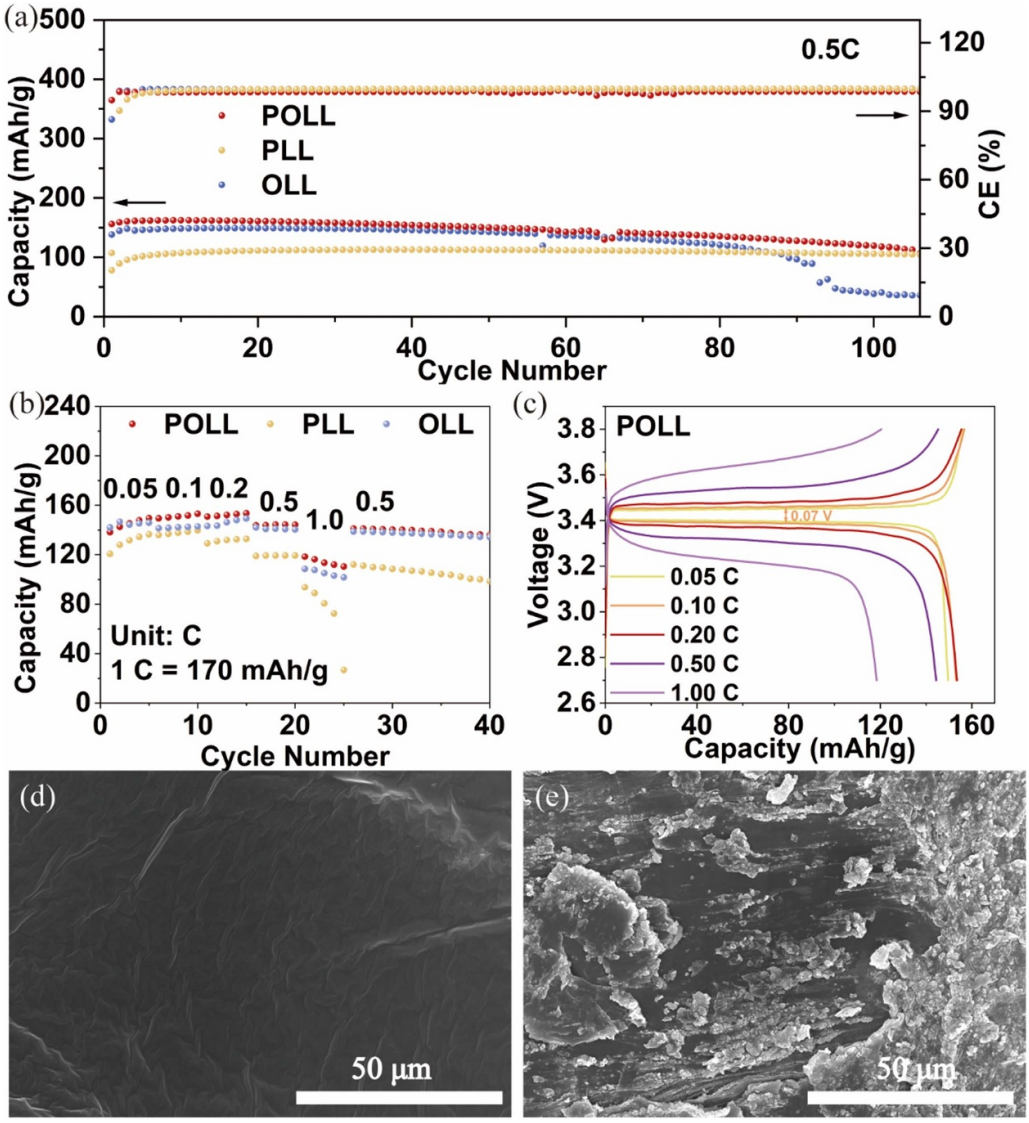

Figure 4. Full cell performance testing. (a) Cycling performance under the current density of 0.5 C. (b) Rate performances. (c) Charge/discharge curves of LFP||POLL||Li cell at various current densities. (d), (e) SEM image of Li anodes after cycles with POLL (d) and OLL (e) electrolytes.

LLZO, whose CCD simply ranges from 0.4 to 1.7 mA cm^{-2} (table S3). It is also common to get an electrochemical window of less than 5 V in the LSV test (table S4). The cycling time of lithium symmetric cells also varies mainly around 1000 h in the similar research (table S5). Consequently, among the previous researches on PCSEs, the POLL in this work shows an impressive CCD, a high electrochemical window, and a long cycling life in lithium symmetric cells (figures 3(f)–(h)), presenting a promising and practical PCSE for ASSBs.

To assess practical performance, the full cells with LFP cathodes and Li anodes were assembled and tested under 0.5 C for POLL, OLL, and PLL (figure 4(a)). Coulombic efficiency almost remains above 99%, indicating reversible Li^+ conduction. OLL shows a significant decline after 90 cycles due to the absence of the nitrile group (–CN), while PLL, despite having abundant –CN, suffers from higher interfacial impedance to reduce the capacity. POLL's initial discharge capacity is 156.1 mAh g^{-1}, decreasing to 119.6 mAh g^{-1} after 100 cycles, retaining 76.6% of its initial capacity. POLL also shows excellent cycling stability without almost capacity fading at 0.2 C for 100 cycles (figure S7). Rate curves (figure 4(b)) show POLL outperforming OLL and PLL, with discharge capacities of 150.0, 153.1, 153.5, 144.2, and 118.5 mAh g^{-1} at 0.05, 0.1, 0.2, 0.5, and 1 C, respectively. When the current density returns to 0.5 C, POLL's capacity remains stable at around 139.0 mAh g^{-1}. The charge and discharge curves for POLL (figure 4(c)) exhibit minimal side reactions, with a voltage difference of 0.07 V at 0.1 C and 0.04 V at 0.05 C, indicating high energy efficiency. Moreover, the volumetric energy densities at 0.1 C are calculated as 338.3, 185.1, and

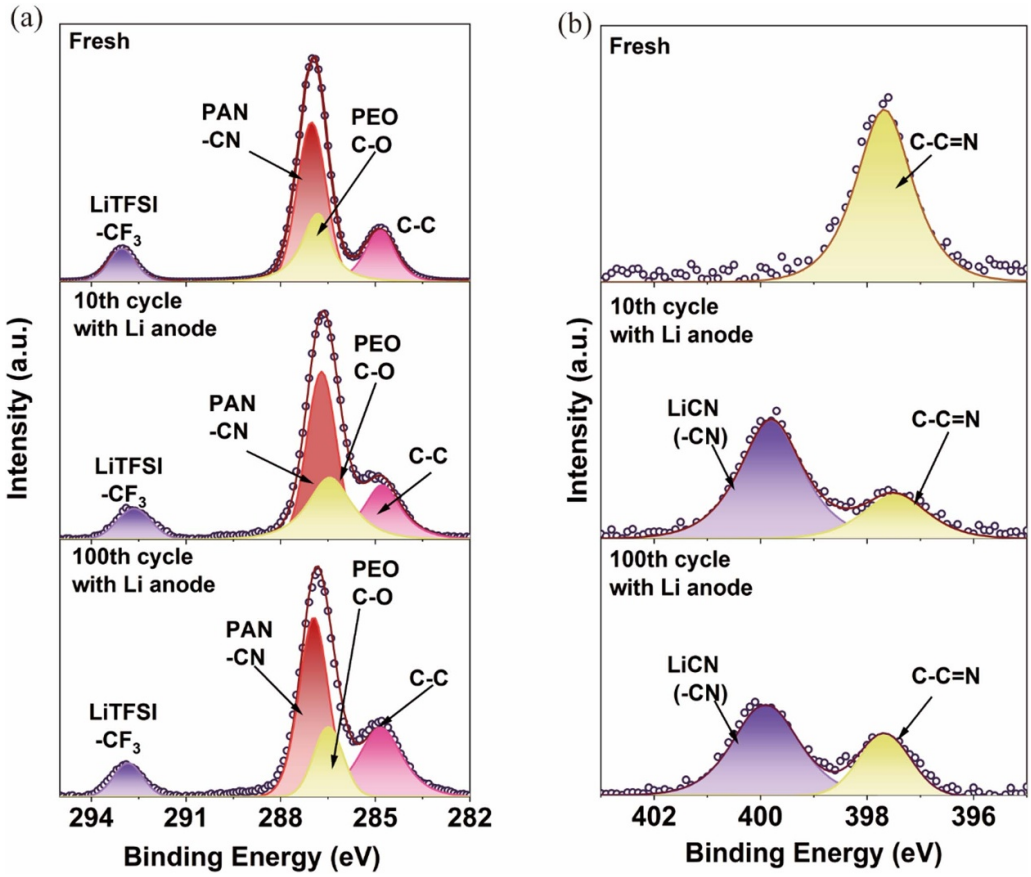

Figure 5. XPS analysis: Fitted spectra of (a) C 1s and (b) N 1s of fresh POLL and POLL-Li interfaces after different cycles.

96.4 Wh L^{-1} for Li||POLL||LFP, Li||OLL||LFP, Li||PLL||LFP, respectively, based on the corresponding charge/discharge curves (figure S8). It shows the significant energy density difference and the importance of fabricating the ultrathin PCSEs. POLL performs far better in volumetric energy density here. SEM images of the lithium-metal interface (figure 4(d)) reveal that POLL maintains a smooth interface without dendrite growth, whereas OLL shows poor contact and particle formation, leading to electric field disorder. PLL has severe interfacial issues with –CN but faces higher impedance due to more evident rugged surfaces (figure S9). The electrochemical stability of POLL is also examined with high-voltage cathode $LiCoO_2$ at 0.2 C with its loads of around 1.5 mg cm^{-2}. The full cells provide first discharge capacities of 167.6 and 135.1 mAh g^{-1} at the cut-off voltages of 4.45 V and 4.2 V (figure S10(a)), respectively, with stable cycling performances (figure S10(b)), indicating good electrochemical stability of POLL at high working voltage.

To reveal the mechanisms of interfacial stability, XPS tests on C and N elements are analyzed at different cycle numbers. As shown in figure 5(a), the C 1s spectra provide detailed information about the polymer and its bonding components in POLL. The C–C (C–H) bonding appears at 284.8 eV, while the –CN is observed at 286.9 eV [37]. The C–O peak at 286.5 eV signifies the presence of PEO, whose stability is likely influenced by its crystallinity. Additionally, the $–CF_3$ group remains stable. The overlapping C–N=C (397.9 eV) and –CN (399.8 eV) peaks suggest that –CN forms during reactions (figure 5(b)). During charge/discharge cycles, lithium reacts with the PAN [38], freeing the nitrile group to enhance Li^+ conduction. The bonding of –CN in LiCN and PAN is balanced to avoid too strong chemical interaction, which impairs the Li^+ transport [39]. The stability of POLL is crucial throughout the electric process, and the C 1s spectra show minimal changes in component ratios, aligning with the performance of ASSBs. The stabilization of the nitrile group after activation further confirms POLL's high Coulombic efficiency and retention capability, which are attributed to negligible side reactions. The electrochemical stability of POLL is significantly enhanced throughout the reaction after the LiCN interlayer formation, attributing to the existence of –CN.

Atomic force microscopy (AFM) images provide insights into the morphology on the surface of fresh and reacted SSEs, highlighting their stability. Similar to SEM results, fresh SSEs have various roughness. POLL is smooth and uniform (figure 6(a)). After cycling under the current density of 0.5 C, POLL maintains close adhesion to the lithium anode, with some POLL adhering to the anode. Reacted POLL retains a dense and smooth structure, indicating stable interfacial contact with the lithium anode (figures 6(b) and (c)). In contrast, OLL is not flat in the fresh state (figure 6(d)). It shows significant morphological changes after cycling, forming noticeable fins across the anode interface in both directions

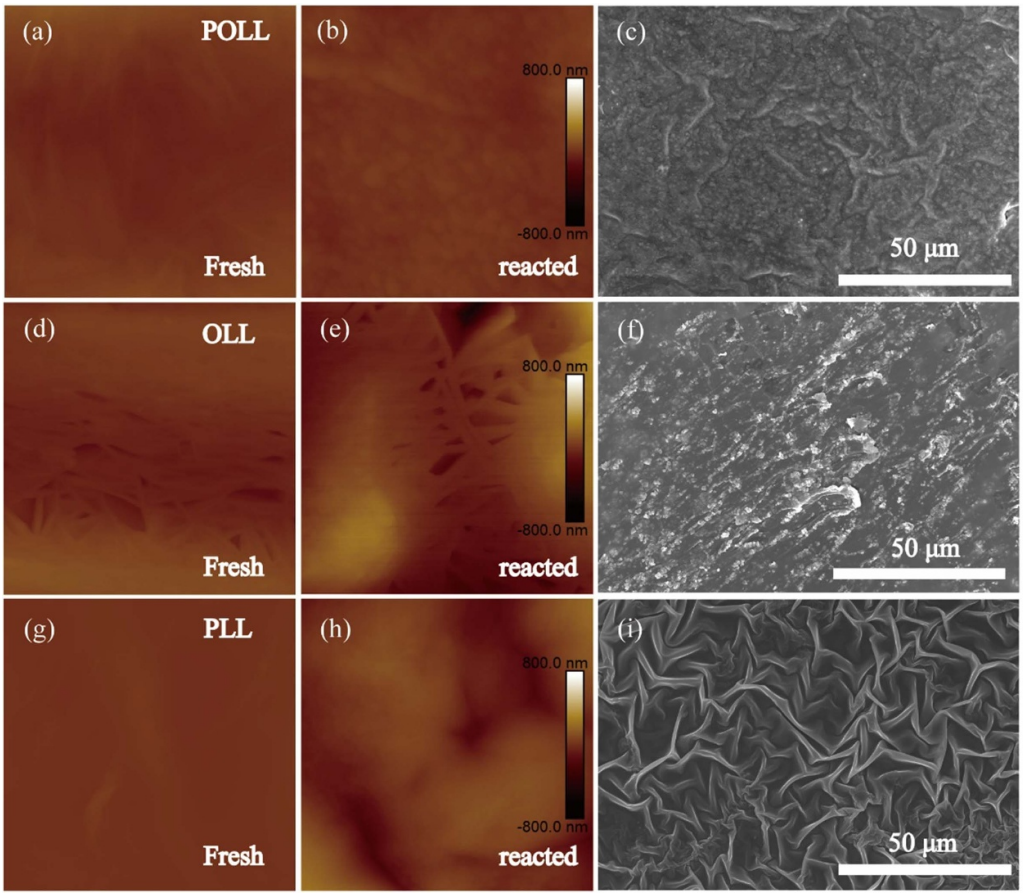

Figure 6. AFM images with a scanning area of 2 × 2 μm on PCSEs (a) fresh POLL without reacting with other materials. (b) Li-anode interface reacted with POLL. (c) SEM images of the interface of POLL cycled with Li-anode. (d) Fresh OLL without reacting with other materials. (e) Li-anode interface reacted with OLL. (f) SEM images of the interface of OLL cycled with Li-anode. (g) Fresh PLL without reacting with other materials. (h) Li-anode interface reacted with PLL. (i) Of the interface of PLL cycled with Li-anode.

(figures 6(e) and (f)). The result suggests that OLL undergoes an evident morphological alteration during cycling, potentially forming vacancies to cause lithium filament growth. PLL is satisfying in smoothness (figure 6(g)). PLL exhibits a comparable good stability after the reaction. The interfaces are not as smooth as POLL's, but no fins grow during the cycling with lithium anode (figures 6(h) and (i)). In brief, the POLL and PLL have more smooth interfaces in the fresh or reacted state, compared to OLL. The AFM morphological results indicate that SSEs with –CN groups offer better stability without visible defects and dendrite growth. Additionally, the incorporation of LLZTO enhances interfacial stability. Overall, POLL demonstrates superior stability in Li^+ transfer within the electrolytes.

4. Conclusion

In summary, we report an effective strategy for fabricating an ultrathin PCSE, utilizing suction filtration with electrospun PAN matrix and electrolyte slurry. With improving the unfavorable mechanical properties, the thickness of the electrolyte is reduced to 12.4 μm in order to restrict internal resistances. The structural design significantly enhances interfacial contact and stabilizes the chemical composition of the PCSE. The dehydrocyanation reaction at the PAN/LLZTO interfaces, combined with the lithium-ion affinity of the nitrile group, facilitates efficient interparticle lithium-ion transport, as evidenced by the apparent activation energy and transference number differences. Furthermore, the LiCN layer on the lithium metal surface and the wide electrochemical window (0–5.5 V) contribute to the exceptional cycling stability. Hence, POLL demonstrates impressive cycling stability performance, including the symmetric cell cycling lifespan of 2100 h and the outstanding CCD of 1.8 mA cm^{-2} without the addition of liquid electrolytes. Furthermore, the full cell utilizing POLL exhibits excellent rate capability and cycling stability over 100 cycles at 0.5 C, with AFM analysis confirming robust interfacial contact between the lithium metal anode and POLL. In addition, the full cells provide a high volumetric energy density of 338.3 Wh L^{-1} at 0.1 C. This work emphasizes the suppression of lithium-dendrite growth

and the improvement of interfacial stability, offering a detailed analysis of the intrinsic properties of PCSEs and a reliable method for manufacturing ultrathin electrolytes.

5. Future perspectives

Ultrathin polymer-based composite SSEs promisingly reduce the impedance of SSEs even with comparable high ionic conductivity. In the PAN/LLZTO/PEO/LiTFSI composite SSE, the LiCN layer forms at the lithium metal–electrolyte interfaces, resulting in long and stable cycling performance. This SSE also exhibits good electrochemical stability under high voltage, as a result of the electrochemical interactions within each component enhancing the electrochemical window. In addition, the SSE in this experiment seems not to be so sensitive to air exposure on a minute scale. Sometimes, LLZTO may expire after being exposed to waste gas in the glove box, indicating specific gases may affect the performance of electrolytes. As an inspiration, future investigations may focus on the inducing stabilization layer by special gas exposure instead of consuming lithium, which may provide an effective method for developing high-performance silicon-based anode all-solid-state LIBs.

Acknowledgment

This work was financially supported by National Natural Science Foundation of China–Chinese Academy of Sciences Frontier Interdisciplinary Assessment Project (XK2023JSC001 and L2324208), Shenzhen Key Laboratory of Advanced Energy Storage (No. ZDSYS20220401141000001), Shenzhen Science and Technology Plan Project (No. SGDX20230116091644003), the Research Grants Council of the Hong Kong Special Administrative Region, China (Project No. R6005-20), and High level of special funds (G03034K001). The authors would also like to acknowledge the technical support from SUSTech Core Research Facilities. The authors thank Xueyanhui (www.xueyanhui.com) for plotting the synthesis diagrams.

Conflict of interest

The authors declare no competing financial interest.

Author's contribution

Fenghua Yu: investigation, methodology, data curation, formal analysis, visualization, writing-original draft. Yongbiao Mu: data curation, writing-review and editing. Meisheng Han: conceptualization, methodology, supervision, writing-review and editing. Jie Liu, Kunxiong Zheng, Zhiyu Zou, Hengyuan Hu, Quanyan Man: data curation, writing-review and editing. Wenjia Li and Lei Wei: writing-review and editing. Lin Zeng: supervision, writing-review and editing. Tianshou Zhao: supervision, funding acquisition, writing-review and editing.

ORCID iDs

Meisheng Han https://orcid.org/0000-0001-9462-3572
Tianshou Zhao https://orcid.org/0000-0003-4825-2381

References

[1] Zhang S *et al* 2023 A family of oxychloride amorphous solid electrolytes for long-cycling all-solid-state lithium batteries *Nat. Commun.* **14** 3780
[2] Liu J, Yuan H, Liu H, Zhao C Z, Lu Y, Cheng X B, Huang J Q and Zhang Q 2022 Unlocking the failure mechanism of solid-state lithium metal batteries *Adv. Energy Mater.* **12** 2100748
[3] Meabe L, Aldalur I, Lindberg S, Arrese-Igor M, Armand M, Martinez-Ibanez M and Zhang H 2023 Solid-state electrolytes for safe rechargeable lithium metal batteries: a strategic view *Mater. Futures* **2** 033501
[4] Emley B *et al* 2023 Impact of fabrication methods on binder distribution and charge transport in composite cathodes of all-solid-state batteries *Mater. Futures* **2** 045102
[5] Cui M, Fu S, Yuan S, Jin B, Liu H, Li Y, Gao N and Jiang Q 2023 Dual interface compatibility enabled via composite solid electrolyte with high transference number for long-life all-solid-state lithium metal batteries *Small* **20** 2307505
[6] Duan T, Cheng H, Liu Y, Sun Q, Nie W, Lu X, Dong P and Song M K 2024 A multifunctional Janus layer for LLZTO/PEO composite electrolyte with enhanced interfacial stability in solid-state lithium metal batteries *Energy Storage Mater.* **65** 103091
[7] Okur F *et al* 2023 Intermediate-stage sintered LLZO scaffolds for Li-garnet solid-state batteries *Adv. Energy Mater.* **13** 2203509
[8] Li Z, Zheng W, Lu G, Li M, Tang D, Zhao Q, Wang Y, Xu C and Wang R 2024 Superionic conductor enabled composite lithium with high ionic conductivity and interfacial wettability for solid-state lithium batteries *Adv. Funct. Mater.* **34** 2309751
[9] Fan C, Tufail M K, Zeng C, Mahmood S, Liang X, Yu X, Cao X, Dong Q and Ahmad N 2024 A functional air-stable $Li_{9.8}GeP_{1.7}Sb_{0.3}S_{11.8}I_{0.2}$ superionic conductor for high-performance all-solid-state lithium batteries *ACS Appl. Mater. Interfaces* **16** 28342
[10] Wang Z, Zhao J, Zhang X, Rong Z, Tang Y, Liu X, Zhu L, Zhang L and Huang J 2023 Tailoring lithium concentration in alloy anodes for long cycling and high areal capacity in sulfide-based all solid-state batteries *eScience* **3** 100087
[11] Yao X *et al* 2024 Interface welding via thermal pulse sintering to enable 4.6 V solid-state batteries *Adv. Energy Mater.* **14** 2303422
[12] Xu L *et al* 2021 Garnet solid electrolyte for advanced all-solid-state li batteries *Adv. Energy Mater.* **11** 2000648
[13] Zhang G, Shu J, Xu L, Cai X, Zou W, Du L, Hu S and Mai L 2021 Pancake-like MOF solid-state electrolytes with fast ion migration for high-performance sodium battery *Nano-Micro. Lett.* **13** 105
[14] Ding D, Tao H, Fan X, Yang X and Fan L Z 2024 A hybrid $LiCl/Li_xSn$ conductive interlayer to unlock the potential of solid-state lithium metal batteries *Adv. Funct. Mater.* **34** 2401457
[15] Mu Y *et al* 2024 Highly efficient aligned ion-conducting network and interface chemistries for depolarized all-solid-state lithium metal batteries *Nano-Micro. Lett.* **16** 86
[16] Bai X, Zhao G, Yang G, Wang M, Lin Q and Zhang N 2024 Multifunctional double layer based on regional segregation for stabilized and dendrite-free solid-state li batteries *Adv. Energy Mater.* **14** 2304112

[17] Liang J, Luo J, Sun Q, Yang X, Li R and Sun X 2019 Recent progress on solid-state hybrid electrolytes for solid-state lithium batteries *Energy Storage Mater.* **21** 308

[18] Zhang L, Feng J, Zhu G, Yan J, Bartlett S, Wang Z, Hao Z, Gao Z and Wang R 2024 Effect of $Li_{6.4}La_3Zr_{1.4}Ta_{0.6}O_{12}$ fillers on the interfacial properties between composite PEO-LiTFSI electrolytes with li metal during cycling *ACS Appl. Mater. Interfaces* **16** 13786

[19] Yuan Y, Wang B, Xue K, Ma Y, Liu X, Peng X, Liu M and Lu H 2023 High-voltage solid-state lithium metal batteries with stable anodic and cathodic interfaces by a laminated solid polymer electrolyte *ACS Appl. Mater. Interfaces* **15** 17144

[20] Chen W P *et al* 2021 Bridging interparticle Li^+ conduction in a soft ceramic oxide electrolyte *J. Am. Chem. Soc.* **143** 5717

[21] Hu X, Cheng Y, Dong G, Dong C, Zhang H, Xie J and Xu L 2024 Cation framework nanowires enabling composite solid-state electrolyte with anion exchange platform for rapid Li^+ conduction *Adv. Funct. Mater.* **34** 2316018

[22] Huang H, Liu C, Liu Z, Wu Y, Liu Y, Fan J, Zhang G, Xiong P and Zhu J 2024 Functional inorganic additives in composite solid-state electrolytes for flexible lithium metal batteries *Adv. Powder Mater.* **3** 100141

[23] Han X, Xu M, Gu L-H, Lan C-F, Chen M-F, Lu J-J, Sheng B-F, Wang P, Chen S-Y and Chen J-Z 2024 Monothetic and conductive network and mechanical stress releasing layer on micron-silicon anode enabling high-energy solid-state battery *Rare Met.* **43** 1017

[24] Mu Y *et al* 2024 Constructing robust LiF-enriched interfaces in high-voltage solid-state lithium batteries utilizing tailored oriented ceramic fiber electrolytes *Adv. Energy Mater.* **14** 2400725

[25] Yan H, Hu J, Deng Y X, Hu Y, Zheng J C, Li W, Song T and Dai Y 2024 Long-life high-voltage all-solid-state batteries enabled by bismuth (III)triflate mediated polymer electrolytes *Chem. Eng. J.* **484** 149516

[26] Yin J, Xu X, Jiang S, Wu H, Wei L, Li Y, He J, Xi K and Gao Y 2022 High ionic conductivity PEO-based electrolyte with 3D framework for Dendrite-free solid-state lithium metal batteries at ambient temperature *Chem. Eng. J.* **431** 133352

[27] Gao L, Tang B, Jiang H, Xie Z, Wei J and Zhou Z 2022 Fiber-reinforced composite polymer electrolytes for solid-state lithium batteries *Adv. Sustain. Syst.* **6** 2100389

[28] Huang B, Li Z H, Zhu Y M, Che Y and Wang C A 2022 Tailored lithium metal/polymer electrolyte interface with $LiTa_2PO_8$ fillers in PEO-based composite electrolyte *Rare Met.* **41** 2826

[29] Gao Y, Sun Z, Cui C, Wang H, Cao W, Hou Z, Zhu D, Yang Y and Zhang T 2022 An ultrathin, flexible solid electrolyte with high ionic conductivity enhanced by a mutual promotion mechanism *ACS Appl. Mater. Interfaces* **14** 45373

[30] Shen H, Jing S, Liu S, Huang Y, He F, Liu Y, Zhuang Z, Zhang Z and Liu F 2023 Tailoring the electronic conductivity of high-loading cathode electrodes for practical sulfide-based all-solid-state batteries *Adv. Powder Mater.* **2** 100136

[31] Zhang Z, Fan W, Cui K, Gou J and Huang Y 2024 Design of ultrathin asymmetric composite electrolytes for interfacial stable solid-state lithium-metal batteries *ACS Nano* **18** 17890

[32] Yunker P J, Still T, Lohr M A and Yodh A G 2011 Suppression of the coffee-ring effect by shape-dependent capillary interactions *Nature* **476** 308

[33] Gu J, Chen X, Ma R, He Z, Liang Z, Zhong H, Su Y, Shi J and Yang Y 2023 The insight of micro-short circuits caused by electrochemo-mechanical stress crosstalk in all-solid-state Li metal batteries *Energy Storage Mater.* **63** 103052

[34] Yildirim C, Flatscher F, Ganschow S, Lassnig A, Gammer C, Todt J, Keckes J and Rettenwander D 2024 Understanding the origin of lithium dendrite branching in $Li_{6.5}La_3Zr_{1.5}Ta_{0.5}O_{12}$ solid-state electrolyte via microscopy measurements *Nat. Commun.* **15** 8207

[35] Zhang Z *et al* 2024 Interfacial plasticization strategy enabling a long-cycle-life solid-state lithium metal battery *Small* **20** 2304234

[36] Ye X, Fu H, Zhang Y, Wu D, Zhong Y, Wang X, Ouyang X and Tu J 2024 Modulating the Li-ion transport pathway of succinonitrile-based plastic crystalline electrolytes for solid-state lithium metal batteries *Adv. Funct. Mater.* 2413205

[37] Wang L, Xu S, Wang Z, Yang E, Jiang W, Zhang S, Jian X and Hu F 2023 A nano fiber–gel composite electrolyte with high Li^+ transference number for application in quasi-solid batteries *eScience* **3** 100090

[38] Liu J, Lin H, Li H, Zhao D, Liu W and Tao X 2024 *In situ* polymerization derived from PAN-based porous membrane realizing double-stabilized interface and high ionic conductivity for lithium-metal batteries *ACS Appl. Mater. Interfaces* **16** 21264

[39] Zhou M *et al* 2024 Bimetal fluorides with adjustable vacancy concentration reinforcing ion transport in poly(ethylene oxide) electrolyte *ACS Nano* **18** 26986